Published in final edited form as:
Med Phys. 2008 January ; 35(1): 145–158.

Monte Carlo investigations of megavoltage cone-beam CT using thick, segmented scintillating detectors for soft tissue visualization

Yi Wang, **Larry E Antonuk**, **Youcef El-Mohri**, **Qihua Zhao**, **Amit Sawant**, and **Hong Du**
Department of Radiation Oncology University of Michigan, Ann Arbor, MI 48103

Abstract

Megavoltage cone-beam computed tomography (MY CBCT) is a highly promising technique for providing volumetric patient position information in the radiation treatment room. Such information has the potential to greatly assist in registering the patient to the planned treatment position, helping to ensure accurate delivery of the high energy therapy beam to the tumor volume while sparing the surrounding normal tissues. Presently, CBCT systems using conventional MV active matrix flat-panel imagers (AMFPIs), which are commonly used in portal imaging, require a relatively large amount of dose to create images that are clinically useful. This is due to the fact that the phosphor screen detector employed in conventional MV AMFPIs utilizes only ~2% of the incident radiation (for a 6 MV x-ray spectrum). Fortunately, thick, segmented scintillating detectors can overcome this limitation, and the first prototype imager has demonstrated highly promising performance for projection imaging at low doses. It is therefore of definite interest to examine the potential performance of such thick, segmented scintillating detectors for MV CBCT. In this study, Monte Carlo simulations of radiation energy deposition were used to examine reconstructed images of cylindrical CT contrast phantoms, embedded with tissue-equivalent objects. The phantoms were scanned at 6 MV using segmented detectors having various design parameters (*i.e.*, detector thickness, as well as scintillator and septal wall materials). Due to constraints imposed by the nature of this study, the size of the phantoms was limited to ~6 cm. For such phantoms, the simulation results suggest that a 40 mm thick, segmented CsI detector with low density septal walls can delineate electron density differences of ~2.3% and 1.3% at doses of 1.54 and 3.08 cGy, respectively. In addition, it was found that segmented detectors with greater thickness, higher density scintillator material, or lower density septal walls exhibit higher contrast-to-noise performance. Finally, the performance of various segmented detectors obtained at a relatively low dose (1.54 cGy) was compared to that of a phosphor screen similar to that employed in conventional MV AMFPIs. This comparison indicates that, for a phosphor screen to achieve the same contrast-to-noise performance as the segmented detectors, ~18 to 59 times more dose is required, depending on the configuration of the segmented detectors.

Keywords

active matrix flat-panel imager; segmented scintillating detectors; megavoltage cone-beam CT; soft tissue visualization; contrast-to-noise ratio

I. INTRODUCTION

Technical advances in radiation therapy, such as three-dimensional conformal[1] and intensity modulated radiation therapy[2], have created the possibility of delivering treatment beams ever more precisely, leading to increased dose to tumor volumes and significant dose reduction to surrounding normal tissues and critical structures. However, the successful execution of high precision radiation treatments relies on accurate patient set-up in the treatment room so as to ensure the dose is delivered as intended.[3] For this reason, a variety of volumetric imaging techniques are under investigation to provide tumor volume visualization in the treatment room immediately before the treatment.[4-17] One such technique that has been clinically implemented involves acquiring cone-beam computed tomography (CBCT) images with a kilovoltage (kV) x-ray source and a diagnostic active matrix flat-panel imager (AMFPI), both orthogonally mounted to the treatment gantry.[5-11] This system can produce useful CT images at clinically acceptable doses (*i.e.*, a few cGy, which is approximately equal to the dose for one portal image).[8-10]

Another CT imaging technique that is also under investigation for soft tissue visualization involves the use of the megavoltage (MV) therapy beam and an electronic portal imaging device (EPID).[5-8,11,18-32] Although the intrinsic contrast of human anatomical structures is lower at MV energies compared to kV energies, it has been demonstrated that soft tissues can be visualized on MV CBCT images obtained using conventional, as well as investigational, imagers.[8,24,30,33] In addition, MV CBCT can offer some advantages over the kV technique. For example, MV CBCT makes use of the therapy beam itself and of a MV AMFPI that has already been installed for portal imaging, without need for additional equipment.[34] Also, MV CBCT images can, in principle, be directly used for high accuracy dose calculation[16,22,35] and inhomogeneity corrections[36]. Furthermore, MV CBCT is almost free of the "streak artifacts" that can occur at kV energies when metal objects, such as dental fillings and hip prostheses, are present in the imaged volume.[21,37] Finally, MV CBCT is much less subject to scatter radiation which can degrade the image quality of kV CBCT.[22]

Despite these advantages, clinical implementation of MV CBCT is constrained by the relatively low quantum efficiency (*i.e.*, less than 2% at 6 MV) of the phosphor screen + metal plate x-ray detectors used in conventional megavoltage AMFPIs.[38,39] As a result, the dose needed for soft tissue visualization with such conventional imagers is relatively high. For example, Groh *et al.* have reported the use of 32 cGy to delineate ~4% density differences.[8] Also, Morin *et al.* have reported using 14.4 cGy to obtain pelvic images with visible soft tissues (*e.g.*, prostate, rectum, fat, and muscle)[22], and 9 MU to obtain pelvic images having sufficient soft tissue information to guide 3D positioning[23]. If the x-ray detector quantum efficiency could be greatly improved, it is reasonable to expect that soft tissues could be visualized at considerably lower, clinically acceptable doses using megavoltage cone-beam (or fan-beam) CT. For this reason, high efficiency x-ray detectors have been widely investigated. For example, one-dimensional linear, as well as arc, detectors incorporating thick Xenon gas ionization chambers[32,33,40] and thick crystalline scintillating detectors have been constructed and evaluated.[41-45] Moreover, a two-dimensional (2D) matrix of 10 mm thick crystalline CsI(T1) scintillating detector coupled with a TV camera has been examined.[46,47] In addition, an AMFPI-based system incorporating a 2D matrix of 8 mm thick CsI(T1) crystals (but with a much finer pitch and larger area than the camera system) has been developed,[25] and recently used for lung tumor imaging and respiratory gating.[26-28] Also, the feasibility of using thick optical fibers to detect Cerenkov radiation has been discussed.[48] An alternative means for improving MV CBCT performance is to modify the treatment beam so as to generate lower energy X rays for imaging. This is currently under investigation through replacement of the usual tungsten target with a target made of low Z material (*e.g.*, carbon) and removing the flattening filter during image acquisition.[49]

Towards greatly increasing the x-ray detector efficiency of megavoltage imagers, initial theoretical and empirical investigations of up to 40 mm thick, segmented crystalline scintillating detectors have recently been reported by our group.[50,51] A prototype AMFPI incorporating such a detector design has been constructed and demonstrated highly promising performance at low doses.[51] These promising early results motivate the present investigation of the potential performance of such detector designs for MV CBCT.

In this paper, Monte Carlo methods simulating x-ray energy deposition are used to theoretically examine the contrast, noise and contrast-to-noise performance of MV CBCT systems incorporating various segmented scintillating detector designs. The resulting performance is then compared to that from a simulated MV CBCT system employing a phosphor screen detector. The simulations suggest that soft tissue visualization can be achieved in MV CBCT images at clinically acceptable doses. Finally, prospects for realization of optimized detector configurations for low dose MV CBCT are discussed.

II. METHODS

In order to quantify the performance of MV CBCT systems incorporating a variety of hypothetical segmented scintillating detector configurations, Monte Carlo simulation of energy deposited by the incident radiation was employed. (Optical transport simulation was beyond the scope of this study.)

A. Simulation set-up

Figure 1 illustrates the simulated MV CBCT system. A point x-ray source and a segmented scintillating detector were used to scan a cylindrical CT contrast phantom tomographically. The x-ray source employed a 6 MV photon beam representing a typical spectral output along the central axis of a Varian linear accelerator.[52] Any changes in the spectral output across the radiation field caused by the shape of the accelerator's flattening filter were not considered in the present simulations. However, for the small field size used in the study, these changes are minimal[53] and would not significantly affect the results of the simulation. The center of the phantom and the entrance surface of the detector were 126 and 130 cm from the source, respectively. The detector had an area of 9.14 × 4.12 cm^2. The beam size at the entrance of the detector was 8.46 × 3.17 cm^2, which covered the whole CT contrast phantom in the radial direction. The segmented scintillating detector consisted of a matrix of 180 × 81 scintillator elements separated by septal walls and a 1 mm thick copper plate coupled to the x-ray side of the scintillator matrix acting as a radiation buildup layer. In this study, 10 and 40 mm thick, segmented CsI and BGO detectors, separated with low density (polystyrene), equivalent density (scintillator material) and high density (tungsten) septal walls were examined, for a total of 12 detector configurations. The detector element-to-element pitch was chosen to be 0.508 mm, equal to the pixel pitch of an indirect-detection MV AMFPI array[54] that has been used in empirical evaluation of a recent prototype[51]. The width of the septal walls was chosen to be 0.05 mm, corresponding to the minimum value that can be achieved with present fabrication techniques. In the simulations, the energy deposited in the septal walls was not considered to contribute to the imaging signal, even in the cases where the septal walls were assumed to be the same material as the scintillator. The use of the three septal wall types allowed examination of detector performance when the scintillator and the septal walls have greatly different, as well as similar, radiation attenuation properties. Ideally, the scintillator elements should be focused towards the x-ray source,[50] so as to reduce the loss of spatial resolution induced by the X rays incident at oblique angles. For the present study however, due to the large source-to-detector distance and the limited detector size, the maximum incident angle of the X rays is only ~2°. Therefore, the simulated system does not suffer greatly from the effect of oblique incidence of radiation, and thus, for reasons of simplicity, a non-focused geometry was used.

For comparison, CBCT simulations were also performed with a conventional MV AMFPI incorporating a phosphor screen detector, which consisted of a Gd_2O_2S:Tb screen (surface density of 133 mg/cm^2) and an overlying 1 mm thick copper plate.[39] The screen had the same area as the segmented scintillators, and was considered to consist of 180 × 81 voxels, with a voxel pitch of 0.508 mm. The energy deposited in each voxel was taken as the imaging signal.

Figure 2 schematically illustrates the simulated CT contrast phantoms, each of which consists of one or three cylindrical tissue-equivalent objects embedded in a large “background” water cylinder. The diameters of the object cylinders and the large water cylinder were 2.03 and 6.10 cm, respectively. The center of each object cylinder was positioned 1.52 cm from the center of the water cylinder. The length of all phantoms was 4.06 cm. In this study, due to a limitation on the maximum number of array elements allowed by the simulation codes, it was not feasible to use segmented detectors with an element pitch of 0.508 mm to perform tomographic scans of CT contrast phantoms of human dimensions (*e.g.*, 20 to 30 cm). Fig. 2(a) illustrates a phantom with a single embedded object. This phantom, which was used in six sets of simulations involving six tissue-equivalent materials, was scanned with a 40 mm thick, segmented CsI detector with low density septal walls. The chemical compositions and physical properties of these materials are summarized in Table I. Fig. 2(b) shows a phantom with three objects which was scanned with the various x-ray detectors. The three tissue equivalent objects were liver, brain, and breast, whose properties appear in Table I. The use of the three-object phantom to perform simulations involving these three materials considerably reduced the total amount of computational time required for this part of the study.

B. Monte Carlo simulations

EGSnrc[57] and DOSXYZnrc[58] Monte Carlo codes were used to simulate radiation energy deposition in various x-ray detectors. In the simulations, the parameters of PCUT and ECUT (corresponding to cutoff energies for photons and electrons) were chosen to be 0.01 and 0.521 MeV (corresponding to a kinetic energy of 0.01 MeV), respectively. The EXACT boundary crossing algorithm, PRESTA-II electron-step algorithm, and NIST bremsstrahlung cross sections were used. The simulations were performed using a total of 264 CPUs on two 64-bit Linux clusters with 1.8 and 2.2 GHz AMD Opteron processors, respectively, as well as a 64-bit Apple cluster with 2.0 GHz G5 processors. This study required a total of ~700,000 CPU hours.

1. X-ray fluence to dose correspondence—In this study, the amount of radiation used in the CBCT simulations was quantified in terms of the x-ray fluence (*i.e.*, the number of X rays per unit area) incident on the phantom. In order to allow comparison of the irradiation conditions used in the simulations to those reported in other publications concerning MV CBCT, the equivalence between the x-ray fluence and the irradiation time [in monitor units (MU)] for a therapy machine was established through a calibration simulation of the absorbed dose (in cGy) at a depth of 10 cm, in a 30 × 30 × 30 cm^3 water phantom. The surface of the water phantom was positioned 100 cm from the source, and the field size at the surface was 10 × 10 cm^2. Under such calibration conditions and for an irradiation time of 1 MU, a medical linac is typically calibrated so as to deposit ~0.8 to 1 cGy of dose at 6 MV. Therefore, the doses reported in this paper correspond to the irradiation time (in monitor units) for therapy machines so calibrated, and thus represent equivalent calibration doses. (For simplicity, in this paper, such equivalent calibration doses will be referred to, simply, as doses.) The calibration simulation was performed using 20×10^9 X rays crossing the 10 × 10 cm^2 field at 100 cm and yielded a dose of ~0.09 cGy, with a statistical uncertainty of ~0.6%. The x-ray fluence used in this calibration simulation corresponds to a value for 3.17×10^9 X rays over the 8.46 × 3.17 cm^2 field at 130 cm (where the CBCT simulations were performed). Thereafter, for a given CBCT simulation using N X rays, the corresponding dose is given by:

$$Dose = \frac{N}{3.17 \times 10^9} \times 0.09 \quad (\text{cGy})\,. \tag{1}$$

For example, for the simulations involving the segmented scintillating detectors, 0.6 × 10^9 X rays were used for each of 180 projection images, resulting in a total scan dose of 3.08 cGy. For the simulations involving the phosphor screen detector, 19.8 × 10^9 X rays were used per projection, resulting in a total scan dose of 101.64 cGy.

2. Cupping artifact removal—A cupping artifact, arising from radiation scattering,[9,59,60] was observed on the reconstructed images. This artifact was manifested as a general increase in signal along the radial direction from the center to the edge of the cylindrical CT phantom. A standard method to remove this artifact involves determination and subtraction of correction factors based on the averaged radial signal in the reconstructed image of a uniform water phantom having the same dimensions as the contrast phantom and obtained using the same simulation set-up.[61] However, this method was impractical to implement for all detector configurations studied. Since each configuration required its own correction, which consumes as much computational time as scanning the contrast phantom, an additional ~500,000 CPU hours would have been required for all configurations. This was beyond the resources available to the study. For that reason, a simplified determination method was developed. Instead of simulating an additional uniform water phantom, the simplified method involved the use of the water region in the reconstructed image of the contrast phantom itself to obtain the correction factors. For validation purpose, both methods were examined and compared for the case of a 40 mm thick, segmented CsI detector with low density septal walls.

3. Performance evaluation—The Monte Carlo investigations presented in this paper consist of evaluation of MV CBCT systems incorporating various segmented scintillating detectors and a phosphor screen detector. A 40 mm thick, segmented CsI detector with low density septal walls was chosen to examine system performance as a function of slice thickness ranging from 1 mm to 20 mm, as well as for total scan doses ranging from 1.54 to 6.16 cGy. The same detector was also used to study a variety of tissue-equivalent materials at 1.54 and 3.08 cGy. In addition, three tissue-equivalent materials (*i.e.*, liver, brain and breast) were chosen to be scanned using the various segmented detectors with different detector thicknesses, scintillator materials and septal wall materials, at 3.08 cGy. The same three materials were also studied at much higher doses (up to 101.64 cGy) using the phosphor screen detector, the performance of which was compared to that of the segmented detectors at 1.54 cGy.

C. Analysis methods

Each CT contrast phantom was scanned over 360 degrees, at 2-degree intervals, resulting in a total of 180 projection images. A Feldkamp-based algorithm using a ramp filter,[62] which employs attenuation line integrals (l) along straight pathways from the source to the imager pixels, was used to reconstruct the spatial distribution of attenuation coefficients for the CT phantoms. At each projection angle, l can be calculated using the exponential attenuation formula,

$$\frac{I_1}{I_0} = e^{-l} \Rightarrow l = \ln\frac{I_0}{I_1}, \tag{2}$$

where I_1 and I_0 are x-ray intensity signals obtained from projection images with and without the phantom, respectively. In order to minimize the statistical error induced by I_0, 30 flood-field images (*i.e.*, images acquired without a phantom), each obtained with the same dose as that used for a phantom image, were averaged. For each scan, one averaged flood-field image was used for all projection angles. The reconstructed voxel pitch and single slice thickness were chosen to be 0.508 mm, matching the pixel pitch of the AMFPI array.[54] From the reconstructed image, a number of single slices were averaged to obtain a slice image with better statistics (*e.g.*, 5.08 mm for 10 slices).

In the reconstructed images, the mean signals in the water background (μ_{water}) and in the object (μ_{obj}) were extracted to evaluate performance. The selection of the regions from which data were extracted excluded the edges of the objects and the phantom, as well as the center of the phantom where the cupping artifact correction induced non-negligible statistical uncertainties. [See Eq. (A5) in the Appendix.]

The deduced signal and noise are expressed in units of MV CT number, assuming a value of 0 Hounsfield Units (HU) in water, and –1000 HU in air (or vacuum). Metrics evaluated in this study include contrast (*Contrast*), noise (*Noise*), and contrast-to-noise ratio (*CNR*) of the tissue-equivalent objects in the reconstructed images. The *Contrast* of the object can be expressed as

$$Contrast=\frac{\left|\mu_{obj}-\mu_{water}\right|}{\mu_{water}}\times 1000 \quad (\mathrm{HU}). \tag{3}$$

Similarly, the *Noise* in the object can be expressed as

$$Noise=\frac{\sigma_{obj}}{\mu_{water}}\times 1000 \quad (\mathrm{HU}), \tag{4}$$

where σ_{obj} is the standard deviation of the voxel signal in the object. Therefore, the *CNR* of the object can be expressed as

$$CNR=\frac{Contrast}{Noise}=\frac{\left|\mu_{obj}-\mu_{water}\right|}{\sigma_{obj}}. \tag{5}$$

The statistical uncertainties in the performance metrics were examined using a previously described method for CT imaging.[63] The details of the statistical uncertainty analysis can be found in the Appendix.

III. RESULTS

A. Cupping artifact removal

Figure 3 shows reconstructed images of a three-object phantom [as illustrated in Fig. 2(b)] before and after the application of the standard method for cupping artifact removal. The reconstructed images and the correction factors for cupping artifact removal were obtained using a 40 mm thick, segmented CsI detector with low density septal walls. Since the standard method requires the acquisition of independent CT scans with a uniform water cylinder so as to obtain correction factors, it was not practical to apply to all detector configurations. Instead, a simplified method based on acquiring the correction factors from the CT phantom images themselves was employed. In order to validate this simplified method, the correction factors obtained using this method were compared to those obtained using the standard method, as illustrated in Fig. 4. The factors obtained using both methods are very similar, indicating that they are equally effective in removing the cupping artifact. Moreover, the *CNR* results calculated from images corrected with both methods differed by only ~2%, which is much lower than the ~7% statistical error in the *CNR* results. Therefore, the simplified method can be used as a valid estimation for removing the cupping artifact. In the remainder of the Results section, the simplified method will be applied unless otherwise stated.

B. Performance evaluation

1. Slice thickness and total scan dose—The 40 mm thick, segmented CsI detector with low density septal walls was selected to demonstrate the square of *CNR* (CNR^2) performance as a function of the slice thickness and total scan dose. Fig. 5(a) illustrates CNR^2 performance as a function of slice thickness (up to 20 mm) at a total scan dose of 3.08 cGy. The CNR^2 results are shown to exhibit a linear increase with increasing slice thickness. Fig. 5(b) illustrates CNR^2 performance as a function of total scan dose (up to 6.16 cGy) for a slice thickness of 5.08 mm. These CNR^2 results also exhibit a linear increase with increasing total scan dose. The linear behaviors observed in Figs. 5(a) and 5(b) are both due to the linear decrease in the square of *Noise* ($Noise^2$) in the objects with increasing number of sampled quanta - resulting in improved statistics. In the remainder of the Results section, performance metrics will be examined with a 5.08 mm thick reconstructed slice (obtained by averaging 10 consecutive, individual slices), and the segmented detectors will be examined at 1.54 and 3.08 cGy.

2. Tissue-equivalent objects—The CT contrast phantoms embedded with various tissue-equivalent objects [as illustrated in Fig. 2(a)] were examined using the 40 mm thick, segmented CsI detector with low density septal walls. In this case, the effect of the cupping artifact was removed using the standard method. Fig. 6(a) illustrates results for *Contrast* at 3.08 cGy and *Noise* at 1.54 and 3.08 cGy, plotted as a function of the relative electron density of the various tissue-equivalent objects. The *Contrast* results at 1.54 cGy are almost the same as those at 3.08 cGy, and are not plotted for reasons of clarity of presentation. For the low contrast tissue-equivalent objects that have been examined, the *Contrast* results increase approximately linearly with increasing difference in relative electron density between the objects and the water background, due to the dominant effect of Compton scattering at megavoltage energies. The slight deviations from linear behavior are due to the presence of lower probability interactions caused by pair production, whose probability is not proportional to the electron density. In addition, it is found that within the range of statistical uncertainty, the *Noise* performance is independent of the relative electron density for the tissue-equivalent objects studied. The reduced level of *Noise* for the higher dose is due to the larger number of X rays sampled. Fig. 6(b) illustrates the *CNR* performance of the tissue-equivalent objects. The *CNR* results increase in a pattern similar to that observed for the *Contrast* results. The improvement in *CNR* at the higher dose is due to a reduced level of *Noise*. Fig. 7 shows the reconstructed images of the CT contrast phantoms incorporating the various objects at 1.54 and 3.08 cGy. As illustrated, it is possible for the segmented detector to delineate 2.3% [Fig. 7(b)] and 1.3% [Fig. 7(i)] electron density difference at 1.54 and 3.08 cGy, respectively. Also, it is observed that the visibility of the tissue-equivalent objects improves with dose and with the relative electron density difference between each object and water, as expected and in line with the *CNR* results of Fig. 6(b).

3. Segmented scintillating detector configurations—Segmented scintillating detectors with different detector thicknesses, scintillator materials and septal wall materials were examined at 3.08 cGy using the three-object CT contrast phantom [as illustrated in Fig.

2(b)]. Fig. 8 illustrates *Contrast*, *Noise* and *CNR* performance of the three tissue-equivalent objects. The *Contrast* performance is mainly determined by the relative electron density of the object. It is observed that the thicker detectors exhibit slightly lower *Contrast*, probably due to the increased relative contribution of phantom scatter radiation to detector signal. Since scatter radiation is lower in energy compared to the primary radiation, it is more efficiently absorbed as detector thickness increases. The effect of the scintillator and septal wall materials on *Contrast* is not pronounced. The *Noise* performance is mainly determined by the detector properties. In general, detectors with greater thickness, higher density scintillator and lower density septal walls, provide lower *Noise*. The *Noise* values of the three objects scanned with the same detector are observed to be equivalent within the range of statistical uncertainty. Generally, it is found that detectors with greater thickness, higher density scintillator and lower density septal walls offer higher *CNR* performance for a given object, mainly due to the reduced level of *Noise*.

Figure 9 shows CNR^2 results for the liver-equivalent object obtained using segmented detectors with low and high density septal walls. These results, obtained at 3.08 cGy, are plotted as a function of the zero frequency *DQE* of the corresponding detectors. These *DQE* values were reported in a previous Monte Carlo-based study.[50] As shown in the figure, for detectors with the same septal wall density (*i.e.*, low or high), CNR^2 increases with increasing *DQE*. Moreover, it is found that, for a given combination of detector thickness and scintillator material (*e.g.*, 40 mm BGO), the detectors with higher density septal walls exhibit lower CNR^2 performance, despite providing a higher *DQE*. This behavior is a consequence of the fact that higher density septal walls provide a higher degree of radiation attenuation. On the one hand, this higher attenuation results in higher x-ray quantum efficiency, leading to a better *DQE* performance. On the other hand, the higher attenuation also limits the lateral spread of the radiation and reduces the effect of statistical averaging, leading to larger variation of the voxel signals in the reconstructed image (*i.e.*, $Noise^2$), and thus lower CNR^2 performance.

Figure 10 shows reconstructed images of the three-object phantom obtained using the various segmented scintillating detectors at 3.08 cGy. As illustrated, the three objects are clearly visible on all reconstructed images. In addition, the visibility of the objects improves with increasing detector thickness and scintillator density, and with decreasing septal wall density, in line with the *CNR* results of Fig. 8.

4. Segmented detectors versus phosphor screen—In this section, the performance obtained using the various segmented scintillating detectors is compared to that obtained using a phosphor screen detector whose composition is representative of those used in conventional MV AMFPIs. The simulations were performed using the three-object phantom. Fig. 11 shows the CNR^2 performance for the liver-equivalent object as a function of the total scan dose for the 40 mm thick, segmented CsI detector with low density septal walls. The results are compared to those obtained from the phosphor screen detector. The segmented detector exhibits impressive performance, with CNR^2 increasing ~49 times faster with dose than with the phosphor screen detector (1.121 cGy^{-1} compared to 0.023 cGy^{-1}, respectively). Figs. 12(a) and 12(b) show reconstructed images obtained at 4.62 cGy using the same pair of detectors used in Fig. 11. All three objects are clearly visible in Fig. 12(a) (segmented detector), but are almost invisible in Fig. 12(b) (phosphor screen detector).

For the liver-equivalent object, CNR^2 performance of all the segmented scintillating detectors is compared to that of the phosphor screen detector in Fig. 13. The phosphor screen detector performance (solid line) corresponds to the linear fit to the phosphor screen detector results in Fig. 11, and is illustrated as a function of dose (bottom x-axis scale). The plotted values of CNR^2 obtained for the various segmented scintillating detectors at a constant dose of 1.54 cGy (cross symbols) have been positioned along the x-axis direction so as to overlie the phosphor screen detector performance curve. With this plotting convention, the degree of dose reduction provided by the segmented detectors compared to the phosphor screen detector, for an equivalent level of CNR^2 performance, is given by the top x-axis scale. For example, to achieve a CNR^2 performance equivalent to that of the 40 mm thick, segmented BGO detector with low density septal walls at 1.54 cGy, the phosphor screen requires a dose of ~90 cGy. Thus, if the phosphor screen were replaced by such a segmented detector, ~59 times less dose would be required to achieve equivalent CNR^2 performance.

IV. DISCUSSION AND CONCLUSIONS

In this paper, a theoretical evaluation of the performance of thick, segmented scintillating detectors for the visualization of low contrast, soft tissues using MV CBCT at clinically acceptable doses (*e.g.*, ~3 cGy) for a 6 MV x-ray energy spectrum has been reported. Reconstructed images of a water phantom embedded with various tissue-equivalent objects were obtained through simulation of the energy deposited in the scintillating material. The *Contrast*, *Noise* and *CNR* performance were examined as a function of slice thickness, total scan dose, relative electron density of the tissue-equivalent materials and various design parameters of the segmented scintillating detectors. The performance of various segmented detector configurations obtained at a relatively low dose (1.54 cGy) was compared to that of a phosphor screen detector whose composition is representative of those used in conventional MV AMFPIs.

Within the limitation of this study (discussed below), the results indicate that the *Contrast* of a tissue-equivalent object is mainly determined by the difference in relative electron density between the tissue-equivalent object and the water background, due to the dominant effect of Compton scattering at megavoltage energies. The *Contrast* is not largely affected by the properties of the detector. In addition, for the low contrast tissue-equivalent objects that have been examined, and for a given detector, the *Noise* results appear to be independent of the relative electron density within the range of statistical uncertainty. The CNR^2 performance for a tissue-equivalent object exhibits an approximately linear increase with increasing slice thickness and scan dose, due to the reduced $Noise^2$ values induced by the increasing number of X rays sampled. In addition, with the same slice thickness and scan dose, the segmented detectors with greater thickness, higher density scintillators, or lower density septal walls result in lower *Noise*, and thus enhanced *CNR* performance. As seen from the reconstructed images, for the size of the phantoms studied, a 40 mm thick, segmented CsI detector with low density septal walls allows resolution of electron density differences of ~2.3% and 1.3% at 1.54 and 3.08 cGy, respectively. Moreover, all examined segmented detectors can delineate 3.3% electron density difference at 3.08 cGy. In addition, the results also indicate that for a phosphor screen detector to achieve the same CNR^2 performance as the segmented detectors, ~18 to 59 times more dose is required, depending on the configuration of the segmented detector.

Due to constraints imposed by the simulation codes (see Sec. II. A.), the contrast phantoms examined were relatively small (~6 cm in diameter). For larger phantoms, there would be more radiation attenuation and scatter which would be expected to degrade *CNR* performance, so that a higher dose would be required to maintain the same performance obtained from the smaller phantoms. (Additional, exploratory simulations performed on simpler, unsegmented, scintillating detectors suggest that ~3 to 4 times more dose would be required to maintain the same *CNR* performance for a 20 cm phantom.) Nevertheless, it is suspected that, had a larger phantom been used, the *CNR* performance of the segmented detectors relative to the phosphor screen detector would not be significantly affected, since the degree of radiation attenuation and scattering are largely determined by the phantom.

In order to create images that are clinically useful, the CBCT system must have sufficient contrast-to-noise and spatial resolution performance. Table II lists the *CNR* values at 3.08 cGy obtained from this study and the modulation transfer function (*MTF*) values at 0.5 and 1 line pair/mm obtained for the same segmented detector configurations from previous Monte Carlo studies.[50] For comparison, *MTF* values obtained from measurements with a conventional MV AMFPI, with a pixel pitch of 0.508 mm and employing a Lanex Fast B (Eastman Kodak) phosphor screen equivalent to that simulated in the present study, are also shown.[38] The *MTF* values of the segmented detectors are all observed to be higher than that of the phosphor screen at both spatial frequencies, except for the case of the 40 mm thick, segmented CsI detector with low density septal walls at 0.5 line pair/mm. Note that the *MTF* values of the segmented detectors represent the spatial resolution at the center of the detector, where the incident radiation is perpendicular to the detector. The spatial resolution at oblique angles will degrade for detectors with non-focused geometries.[64] Due to the limited area of the radiation field (~8.5 × 3.2 cm^2), the *CNR* results represent radiation incident at very small oblique angles (less than 2°), and is not expected to differ greatly from what would be achieved if focused detector geometries were employed. Therefore, it is anticipated that segmented detectors with focused geometries would provide significantly improved *CNR*, as well as equivalent, or enhanced spatial resolution performance compared to the phosphor screen detectors used in conventional MV AMFPIs.

It must be emphasized that the present study does not include simulation of optical transport in the scintillator. Inclusion of optical transport will certainly affect the *CNR* and *MTF* performance predicted by radiation transport only. For segmented detectors, if the septal walls are made to be optically opaque, the spatial resolution will not be affected by optical transport, but *CNR* will degrade due to optical Swank noise, which originates from depth-dependent variation in the x-ray-to-photon conversion gain. Investigation of this noise source using a recently implemented Monte Carlo package (MANTIS)[65] combining a radiation transport code (PENELOPE-2005)[66] and an optical transport code (DETECT-II)[67] is presently underway. It is anticipated that the optical Swank factor can be made relatively high (>90%) through optimization of detector designs. If the septal walls are not perfectly opaque, element-to-element optical crosstalk will occur, and the spatial resolution of the resulting CT images will degrade. However, the noise level will decrease with increasing optical crosstalk due to increased blurring, resulting in an increase in *CNR*. For the phosphor screen detector, inclusion of optical transport would lead to two competing effects on the *Noise* performance. While lateral spread of optical photons will result in more statistical averaging in the reconstructed images, thereby reducing *Noise*, the corresponding optical Swank factor, which is less than unity, will result in an increase in *Noise*. Therefore, the net effect on *CNR* performance will be determined by the relative magnitude of these two competing effects.

In summary, the results of this study indicate that MV CBCT systems employing thick, segmented scintillating detectors can potentially be used to visualize soft tissue structures at clinically acceptable doses. In order for such detectors to achieve optimum performance for low dose MV CBCT, many design aspects and detector properties will need to be further investigated and optimized – which we believe will be greatly assisted by Monte Carlo simulations of radiation and optical transport.

Acknowledgments

The authors would like to thank Dr. Jeffrey Fessler for providing the cone-beam CT reconstruction algorithm used in this study. We also appreciate Dr. Mahdokht Behravan for her assistance in proofreading. This work was supported by NIH Grant RO1 CA51397.

APPENDIX

For a Monte Carlo simulation using a given detector and phantom combination, the statistical uncertainty in the signal of voxels in a reconstructed image ($\Delta\mu$) can be estimated from the statistical uncertainties in the signal of pixels in projection images (ΔI), using a previously described method.[63] The Monte Carlo simulation can output the pixel signal ($I(x,y,\theta)$) and the relative statistical uncertainty $\left(\frac{\Delta I\,(x,y,\theta)}{I\,(x,y,\theta)}\right)$ associated with that signal for a projection image, where x and y indicate the coordinates of the pixel and θ indicates the projection angle. It is found that, in a projection image, the values of $\frac{\Delta I\,(x,y,\theta)}{I\,(x,y,\theta)}$ were relatively similar for all the pixels in the region of interest. Therefore, a mean value of statistical uncertainty $\left(\frac{\Delta I\,(\theta)}{I\,(\theta)}\right)$, obtained by averaging $\frac{\Delta I\,(x,y,\theta)}{I\,(x,y,\theta)}$ for all the pixels in the region of interest, was used to represent the statistical uncertainty for all the pixels in this projection image. Also, it is observed that, at all projection angles, the values of $\frac{\Delta I\,(\theta)}{I\,(\theta)}$ were almost identical. Therefore, a mean value of statistical uncertainty $\left(\frac{\Delta I}{I}\right)$, obtained by averaging $\frac{\Delta I\,(\theta)}{I\,(\theta)}$ for all the projection angles, was used to represent the statistical uncertainty in the pixel signals in the projection images at all the angles for this simulation.

The line integral (l), as shown in Eq. (2), was obtained from the phantom image signal (I_1) and the averaged flood-field image signal (I_0). Due to the effect of this averaging, the relative statistical uncertainty in I_0 is much smaller than that in I^1. Therefore, the statistical uncertainty in the line integrals (Δl) can be estimated[68] from:

$$\Delta l=\Delta\left(\ln\frac{I_0}{I_1}\right)=\frac{\Delta\left(\frac{I_0}{I_1}\right)}{\frac{I_0}{I_1}}=\sqrt{\left(\frac{\Delta I_0}{I_0}\right)^2+\left(\frac{\Delta I_1}{I_1}\right)^2}\approx\frac{\Delta I_1}{I_1}. \tag{A1}$$

As shown in Eq. (13) of Ref.[63], the root mean square error of the reconstructed voxel signal ($\Delta\mu$) can be expressed using the statistical uncertainty in the line integrals:

$$\Delta\mu=\sqrt{\frac{1.59\times D}{n\times d^3}}\times\Delta l, \tag{A2}$$

where D is the diameter of the reconstructed cylinder (60.96 mm), d is the voxel pitch in the reconstructed image (0.508 mm), and n is the number of coplanar paths, which is equal to the product of the number of projections (180) and the number of AMFPI pixels covering the phantom in the scanning direction (128). With these parameter values and using Eq. (A1), Eq. (A2) becomes:

$$\Delta\mu=0.179\times\frac{\Delta I_1}{I_1}. \tag{A3}$$

In this study, multiple reconstructed slices were averaged to obtain better statistics. The statistical uncertainty in an averaged slice image ($\Delta\mu_s$) can be expressed as:

$$\Delta\mu_s=\frac{\Delta\mu}{\sqrt{n_s}}=\frac{0.179}{\sqrt{n_s}}\times\frac{\Delta I_1}{I_1}, \tag{A4}$$

where n_s is the number of slices averaged.

In addition, the cupping artifact was removed in the averaged slice image using the correction factors $\mu_c(r)$, where r indicate the radial distance from the center of the phantom. The statistical uncertainty in these correction factors [$\Delta\mu_c(r)$] can be expressed as:

$$\Delta\mu_c\,(r)=\frac{\Delta\mu_s}{\sqrt{n_c\,(r)}}=\frac{0.179}{\sqrt{n_c\,(r)\times n_s}}\times\frac{\Delta I_1}{I_1}, \tag{A5}$$

where $n_c(r)$ is the number of voxels averaged for obtaining the correction factor at a radial distance r. In the region selected for evaluation, $n_c(r)$ is at least 32, resulting in values for $\Delta\mu_c(r)$ that are much smaller than for $\Delta\mu_s$. The statistical uncertainty in the voxel signal after cupping artifact removal ($\Delta\mu_{vox}$) can be estimated from $\Delta\mu_s$ and $\Delta\mu_c(r)$:

$$\Delta\mu_{vox}=\sqrt{(\Delta\mu_s)^2+[\Delta\mu_c\,(r)]^2}\approx\Delta\mu_s=\frac{0.179}{\sqrt{n_s}}\times\frac{\Delta I_1}{I_1}. \tag{A6}$$

Therefore, the statistical uncertainties in the mean signal of water background ($\Delta\mu_{water}$) and object ($\Delta\mu_{obj}$) can be expressed as:

$$\Delta\mu_{water}=\frac{\Delta\mu_{vox}}{\sqrt{n_{water}}}=\frac{0.179}{\sqrt{n_s\times n_{water}}}\times\frac{\Delta I_1}{I_1} \tag{A7}$$

and

$$\Delta\mu_{obj}=\frac{\Delta\mu_{vox}}{\sqrt{n_{obj}}}=\frac{0.179}{\sqrt{n_s\times n_{obj}}}\times\frac{\Delta I_1}{I_1}, \tag{A8}$$

where n_{water} and n_{obj} are the number of voxels in the region of the water background and the object, respectively. Note that n_{water} is equal to 7756 for the one-object phantom and 4508 for the three-object phantom, while n_{obj} is equal to 912 for all the examined objects. Moreover, the statistical uncertainty in the standard deviation of the voxel signals in the region of the object ($\Delta\sigma_{obj}$) can be expressed as:

$$\Delta\sigma_{obj}=\Delta\sqrt{\frac{\sum_{i=1}^{n_{obj}}\left(\mu_i-\bar{\mu}\right)^2}{n_{obj}-1}}=\frac{\Delta\mu_{vox}}{\sqrt{n_{obj}-1}}=\frac{0.179}{\sqrt{n_s\times\left(n_{obj}-1\right)}}\times\frac{\Delta I_1}{I_1}. \tag{A9}$$

Therefore, the relative error in the *Contrast* of the object can be expressed as:

$$\frac{\Delta Contrast}{Contrast}=\sqrt{\frac{\left(\Delta\mu_{obj}\right)^2+(\Delta\mu_{water})^2}{\left(\mu_{obj}-\mu_{water}\right)^2}+\left(\frac{\Delta\mu_{water}}{\mu_{water}}\right)^2}. \tag{A10}$$

Furthermore, the relative error in the *Noise* in the region of the object can be expressed as:

$$\frac{\Delta Noise}{Noise}=\sqrt{\left(\frac{\Delta\sigma_{obj}}{\sigma_{obj}}\right)^2+\left(\frac{\Delta\mu_{water}}{\mu_{water}}\right)^2}. \tag{A11}$$

Finally, the relative error in the *CNR* of the object can be expressed as:

$$\frac{\Delta CNR}{CNR}=\sqrt{\frac{\left(\Delta\mu_{obj}\right)^2+(\Delta\mu_{water})^2}{\left(\mu_{obj}-\mu_{water}\right)^2}+\left(\frac{\Delta\sigma_{obj}}{\sigma_{obj}}\right)^2}. \tag{A12}$$

REFERENCES

1. Purdy JA. Advances in three-dimensional treatment planning and conformal dose delivery. Semin. Oncol 1997;24:655–671. [PubMed: 9422262]
2. Purdy JA. Intensity-modulated radiation therapy. Int. J. Radiat. Oncol., Biol., Phys 1996;35:845–846. [PubMed: 8690655]
3. Mackie TR, et al. Image guidance for precise conformal radiotherapy. Int. J. Radiat. Oncol., Biol., Phys 2003;56:89–105. [PubMed: 12694827]
4. Jaffray DA, Drake DG, Moreau M, Martinez AA, Wong JW. A Radiographic and Tomographic Imaging System Integrated into a Medical Linear Accelerator for Localization of Bone and Soft-Tissue Targets. Int. J. Radiat. Oncol., Biol., Phys 1999;45:773–789. [PubMed: 10524434]
5. Jaffray DA, Siewerdsen JH. Cone-beam computed tomography with a flat-panel imager: initial performance characterization. Med. Phys 2000;27:1311–1323. [PubMed: 10902561]
6. Siewerdsen JH, Jaffray DA. Cone-beam computed tomography with a flat-panel imager: magnitude and effects of x-ray scatter. Med. Phys 2001;28:220–231. [PubMed: 11243347]
7. Jaffray DA, Siewerdsen JH, Wong JW, Martinez AA. Flat-panel cone-beam computed tomography for image-guided radiation therapy. Int. J. Radiat. Oncol., Biol., Phys 2002;53:1337–1349. [PubMed: 12128137]
8. Groh BA, Siewerdsen JH, Drake DG, Wong JW, Jaffray DA. A performance comparison of flat-panel imager-based MV and kV cone-beam CT. Med. Phys 2002;29:967–975. [PubMed: 12094992]
9. Graham SA, Moseley DJ, Siewerdsen JH, Jaffray DA. Compensators for dose and scatter management in cone-beam computed tomography. 2007;34:2691–2703.
10. Oelfke U, et al. Linac-integrated kV-cone beam CT: technical features and first applications. Med. Dosim 2006;31:62–70. [PubMed: 16551530]

11. Letourneau D, et al. Cone-beam-CT guided radiation therapy: technical implementation. Radiother. Oncol 2005;75:279–286. [PubMed: 15890424]
12. Barker JL Jr. et al. Quantification of volumetric and geometric changes occurring during fractionated radiotherapy for head-and-neck cancer using an integrated CT/linear accelerator system. Int. J. Radiat. Oncol., Biol., Phys 2004;59:960–970. [PubMed: 15234029]
13. Kuriyama K, et al. A New Irradiation Unit Constructed of Self-Moving Gantry-CT and Linac. Int. J. Radiat. Oncol., Biol., Phys 2003;55:428–435. [PubMed: 12527056]
14. Balter JM, et al. Daily Targeting of Intrahepatic Tumors for Radiotherapy. Int. J. Radiat. Oncol., Biol., Phys 2002;52:266–271. [PubMed: 11777645]
15. Lattanzi J, McNeeley S, Hanlon A, Schultheiss TE, Hanks GE. Ultrasound-Based Stereotactic Guidance of Precision Conformal External Beam Radiation Therapy in Clinically Localized Prostate Cancer. Urology 2000;55:73–78. [PubMed: 10654898]
16. Langen KM, et al. The use of megavoltage CT (MVCT) images for dose recomputations. Phys. Med. Biol 2005;50:4259–4276. [PubMed: 16148392]
17. Meeks SL, et al. Ultrasound-Guided Extracranial Radiosurgery: Technique and Application. Int. J. Radiat. Oncol., Biol., Phys 2003;55:1092–1101. [PubMed: 12605989]
18. Simpson RG, Chen CT, Grubbs EA, Swindell W. A 4-MV CT Scanner for Radiation Therapy: The Prototype System. Med. Phys 1982;9:574–579. [PubMed: 7110089]
19. Swindell W, Simpson RG, Oleson JR, Chen C, Grubbs EA. Computed Tomography with a Linear Accelerator with Radiotherapy Applications. Med. Phys 1983;10:416–420. [PubMed: 6412044]
20. Mosleh-Shirazi MA, Evans PM, Swindell W, Webb S, Partridge M. A cone-beam megavoltage CT scanner for treatment verification in conformal radiotherapy. Radiother. Oncol 1998;48:319–328. [PubMed: 9925252]
21. Pouliot J, et al. Low-dose megavoltage cone-beam CT for radiation therapy. Int. J. Radiat. Oncol., Biol., Phys 2005;61:552–560. [PubMed: 15736320]
22. Morin O, et al. Megavoltage cone-beam CT: system description and clinical applications. Med. Dos 2006;31:51–61.
23. Morin O, et al. Patient dose considerations for routine megavoltage cone-beam CT imaging. Med. Phys 2007;34:1819–1827. [PubMed: 17555263]
24. Ford EC, et al. Cone-beam CT with megavoltage beams and an amorphous silicon electronic portal imaging device: potential for verification of radiotherapy of lung cancer. Med. Phys 2002;29:2913–2924. [PubMed: 12512728]
25. Seppi EJ, et al. Megavoltage cone-beam computed tomography using a high-efficiency image receptor. Med. Phys 2003;55:793–803.
26. Chang J, et al. Integrating respiratory gating into a megavoltage cone-beam CT system. Med. Phys 2006;33:2354–2361. [PubMed: 16898437]
27. Sillanpaa J, et al. Developments in megavoltage cone beam CT with an amorphous silicon EPID: reduction of exposure and synchronization with respiratory gating. Med. Phys 2005;32:819–829. [PubMed: 15839355]
28. Sillanpaa J, et al. Low-dose megavoltage cone-beam computed tomography for lung tumors using a high-efficiency image receptor. Med. Phys 2006;33:3489–3497. [PubMed: 17022245]
29. Hansen EK, et al. Image-guided radiotherapy using megavoltage cone-beam computed tomography for treatment of paraspinous tumors in the presence of orthopedic hardware. Int. J. Radiat. Oncol., Biol., Phys 2006;66:323–326. [PubMed: 16965986]
30. Ghelmansarai FA, et al. Soft Tissue Visualization Using a Highly Efficient Megavoltage Cone Beam CT Imaging System. Proc. SPIE 2005;5745:159–170.
31. Midgley S, Millar RM, Dudson J. A feasibility study for megavoltage cone beam CT using a commercial EPID. Phys. Med. Biol 1998;43:155–169. [PubMed: 9483629]
32. Pang G, Mei X, Rowlands JA. Development of a Novel High Quantum Efficiency Flat Panel Detector for Megavoltage Cone Beam CT/DT: Construction and Evaluation of a Prototype Single-Row Detector. Med. Phys 2006;33:2281.
33. Keller H, et al. Monte Carlo study of a highly efficient gas ionization detector for megavoltage imaging and image-guided radiotherapy. Med. Phys 2002;29:165–175. [PubMed: 11865988]

34. Amols H, Jaffray DA, Orton CG. Image-guided radiotherapy is being overvalued as a clinical tool in radiation oncology. Med. Phys 2006;33:3583–3586. [PubMed: 17089824]

35. Morin O, et al. Dose Calculation Using Megavoltage Cone Beam CT Imaging. Int. J. Radiat. Oncol., Biol., Phys 2005;63:S62–S63.

36. Guan H, Yin FF, Kim JH. Accuracy of inhomogeneity correction in photon radiotherapy from CT scans with different settings. Phys. Med. Biol 2002;47:N223–N231. [PubMed: 12361225]

37. Yin FF, Guan H, Lu W. A technique for on-board CT reconstruction using both kilovoltage and megavoltage beam projections for 3D treatment verification. Med. Phys 2005;32:2819–2826. [PubMed: 16266096]

38. El-Mohri Y, Jee K-W, Antonuk LE, Maolinbay M, Zhao Q. Determination of the Detective Quantum Efficiency of a Prototype, Megavoltage Indirect Detection, Active Matrix Flat-Panel Imager. Med. Phys 2001;28:2538–2550. [PubMed: 11797959]

39. Antonuk LE. Electronic portal imaging devices: A review and historical perspective of contemporary technologies and research. Phys. Med. Biol 2002;47:R3l–R65.

40. Pang G, Rowlands JA. Development of high quantum efficiency, flat panel, thick detectors for megavoltage x-ray imaging: a novel direct-conversion design and its feasibility. Med. Phys 2004;31:3004–3016. [PubMed: 15587653]

41. Morton EJ, Swindell W, Lewis DG, Evans PM. A linear array, scintillation crystal-photodiode detector for megavoltage imaging. Med. Phys 1991;18:681–691. [PubMed: 1921872]

42. Lewis DG, Swindell W, Morton EJ, Evans PM, Xiao ZR. A megavoltage CT scanner for radiotherapy verification. Phys. Med. Biol 1992;37:1985–1999. [PubMed: 1438558]

43. Nakagawa K, et al. Real-time beam monitoring in dynamic conformation therapy. Int. J. Radiat. Oncol., Biol., Phys 1994;30:1233–1238. [PubMed: 7961033]

44. Rathee S, Tu D, Monajemi TT, Rickey DW, Fallone BG. A bench-top megavoltage fan-beam CT using CdWO4-photodiode detectors. I. System description and detector characterization. Med. Phys 2006;33:1078–1089. [PubMed: 16696485]

45. Monajemi TT, Tu D, Fallone BG, Rathee S. A bench-top megavoltage fan-beam CT using CdWO4-photodiode detectors. II. Image performance evaluation. Med. Phys 2006;33:1090–1100. [PubMed: 16696486]

46. Mosleh-Shirazi MA, Swindell W, Evans PM. Optimization of the Scintillation Detector in a Combined 3D Megavoltage CT Scanner and Portal Imager. Med. Phys 1998;25:1880–1890. [PubMed: 9800695]

47. Mosleh-Shirazi MA, et al. Rapid Portal Imaging with a High-Efficiency, Large Field-of-View Detector. Med. Phys 1998;25:2333–2346. [PubMed: 9874825]

48. Mei X, Rowlands JA, Pang G. Electronic portal imaging based on Cerenkov radiation: A new approach and its feasibility. Med. Phys 2006;33:4258–4270. [PubMed: 17153404]

49. Ostapiak OZ, O'Brien PF, Faddegon BA. Megavoltage imaging with low Z targets: implementation and characterization of an investigational system. Med. Phys 1998;25:1910–1918. [PubMed: 9800698]

50. Sawant A, et al. Segmented Crystalline Scintillators: An Initial Investigation of High Quantum Efficiency Detectors for Megavoltage X-Ray Imaging. Med. Phys 2005;32:3067–3083. [PubMed: 16279059]

51. Sawant A, et al. Segmented Crystalline Scintillators: Empirical and Theoretical Investigation of a High Quantum Efficiency EPID Based on an Initial Engineering Prototype CsI(Tl) Detector. Med. Phys 2006;33:1053–1066. [PubMed: 16696482]

52. Sheikh-Bagheri, D. Ph.D. Thesis. Department of Physics, Carleton University; 1999. Monte Carlo Study of Photon Beams from Medical Linear Accelerators: Optimization, Benchmark and Spectra.

53. Yu MK, Sloboda RS, Murray B. Linear accelerator photon beam quality at off-axis points 1997;24:233–239.

54. Antonuk LE, et al. Initial Performance Evaluation of an Indirect-Detection, Active Matrix Flat-Panel Imager (AMFPI) Prototype for Megavoltage Imaging. Int. J. Radiat. Oncol., Biol., Phys 1998;42:437–454. [PubMed: 9788427]

55. Data sheet of tissue characterization phantom (Gammex 467). Gammex RMI Inc.; Wisconsin, U.S.A.: 2006.

56. International Commission on Radiation Units and Measurements (ICRU) Report 46, Photon, Electron, Proton and Neutron Interaction Data for Body Tissues. ICRU Publications; Bethesda, Maryland: 1992.

57. Kawrakow, I.; Rogers, DWO. Technical Report PIRS-701. National Research Council of Canada; Ottawa, Canada: 2000. The EGSnrc Code System: Monte Carlo Simulation of Electron and Photon Transport.

58. Treurniet, JA.; Walters, BRB.; Rogers, DWO. NRC Report PIRS 0623. National Research Council of Canada; Ottawa, Canada: 2001. BEAMnrc, DOSXYZnrc and BEAMDP GUI User's Manual.

59. Glover GH. Compton scatter effects in CT reconstructions. Med. Phys 1982;9:860–867. [PubMed: 7162472]

60. Ning R, et al. Flat panel detector-based cone-beam volume CT angiography imaging: system evaluation. IEEE Trans. Med. Imaging 2000;19:949–963. [PubMed: 11127608]

61. Kachelriess M, Sourbelle K, Kalender WA. Empirical cupping correction: a first-order raw data precorrection for cone-beam computed tomography. Med. Phys 2006;33:1269–1274. [PubMed: 16752561]

62. Feldkamp LA, Davis LC, Kress JW. Practical cone-beam algorithm. J. Opt. Soc. Am. A 1984;1:612–619.

63. Huesman RH. The effects of a finite number of projection angles and finite lateral sampling of projections on the propagation of statistical errors in transverse section reconstruction. Phys. Med. Biol 1977;22:511–521. [PubMed: 866415]

64. Monajemi TT, Fallone BG, Rathee S. Thick, segmented CdWO4-photodiode detector for cone beam megavoltage CT: a Monte Carlo study of system design parameters. Med. Phys 2006;33:4567–4577. [PubMed: 17278808]

65. Badano A, Sempau J. MANTIS: combined x-ray, electron and optical Monte Carlo simulations of indirect radiation imaging systems. Phys. Med. Biol 2006;51:1545–1561. [PubMed: 16510962]

66. Salvat, F.; Fernández-Varea, JM.; Sempau, J. PENELOPE, A code system for monte carlo simulation of electron and photon transport. Issy-les-Moulineaux; France: 2003.

67. Badano, A. Ph.D. Thesis. Center for Integrated Microsystems, University of Michigan; 1999. Image quality degradation by light scattering processes in high performance display devices for medical imaging.

68. Taylor, JR. An Introduction to Error Analysis: The Study of Uncertainties in Physical Measurements. 2nd ed.. University Science Books; California: 1997.

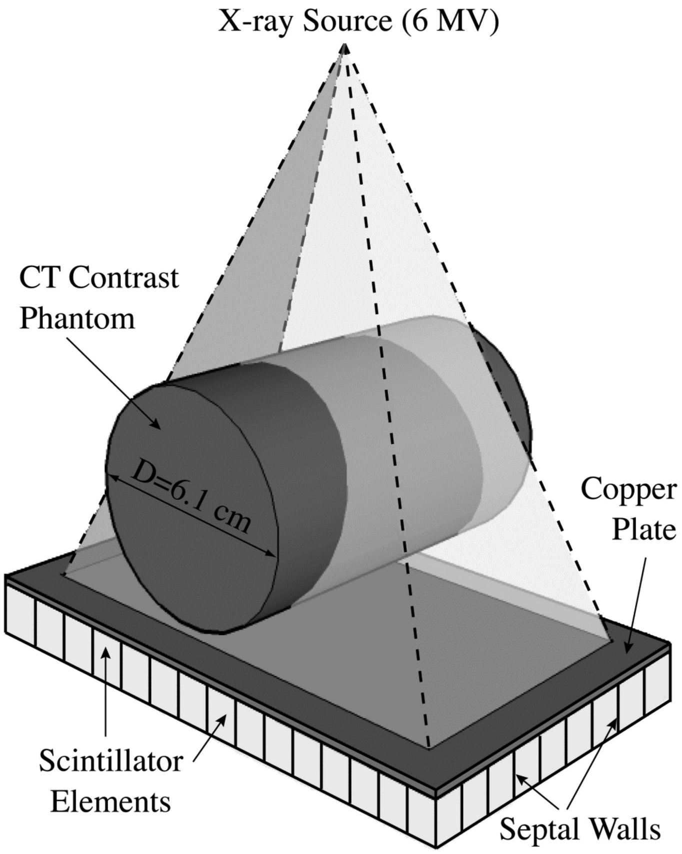

FIG. 1.
Three-dimensional schematic view of the simulated, megavoltage cone-beam CT (MV CBCT) system.

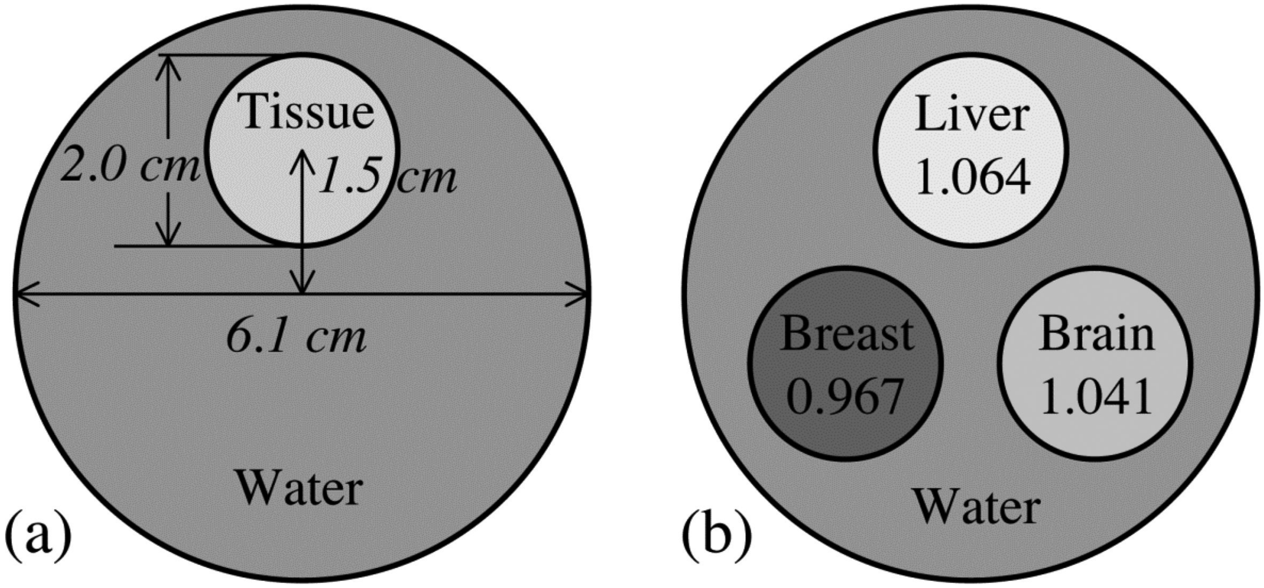

FIG. 2.

Cross-sectional view of the cylindrical CT contrast phantoms simulated in this study. (a) Illustration of a phantom with a single tissue-equivalent object. This phantom, using various tissue-equivalent objects, was employed in the performance evaluation of a 40 mm thick, segmented CsI detector with low density septal walls. (b) Illustration of a phantom with three specific tissue-equivalent objects. The relative electron densities of these objects relative to water are indicated in the figure. This phantom was employed in the performance evaluation of all x-ray detectors examined in this study.

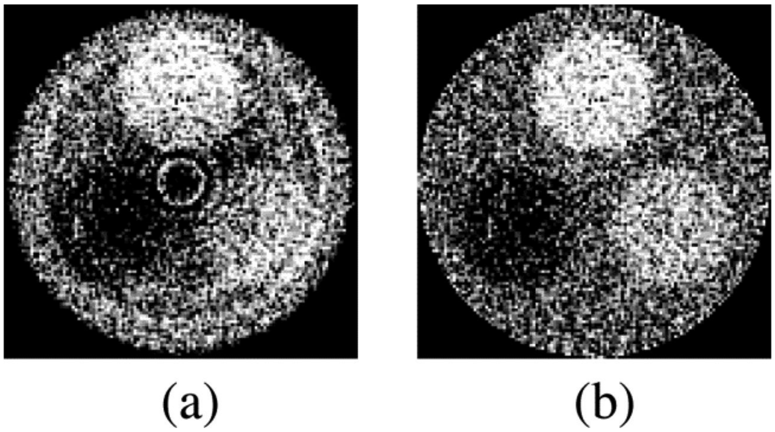

FIG. 3.

Reconstructed images of a three-object CT contrast phantom (a) before and (b) after the correction for a cupping artifact using the standard method (described in the text). The results were obtained using the 40 mm thick segmented CsI detector with low density septal walls. The orientation of the objects in the phantom is the same as that in Fig. 2(b). Note that the same window level was selected for both images.

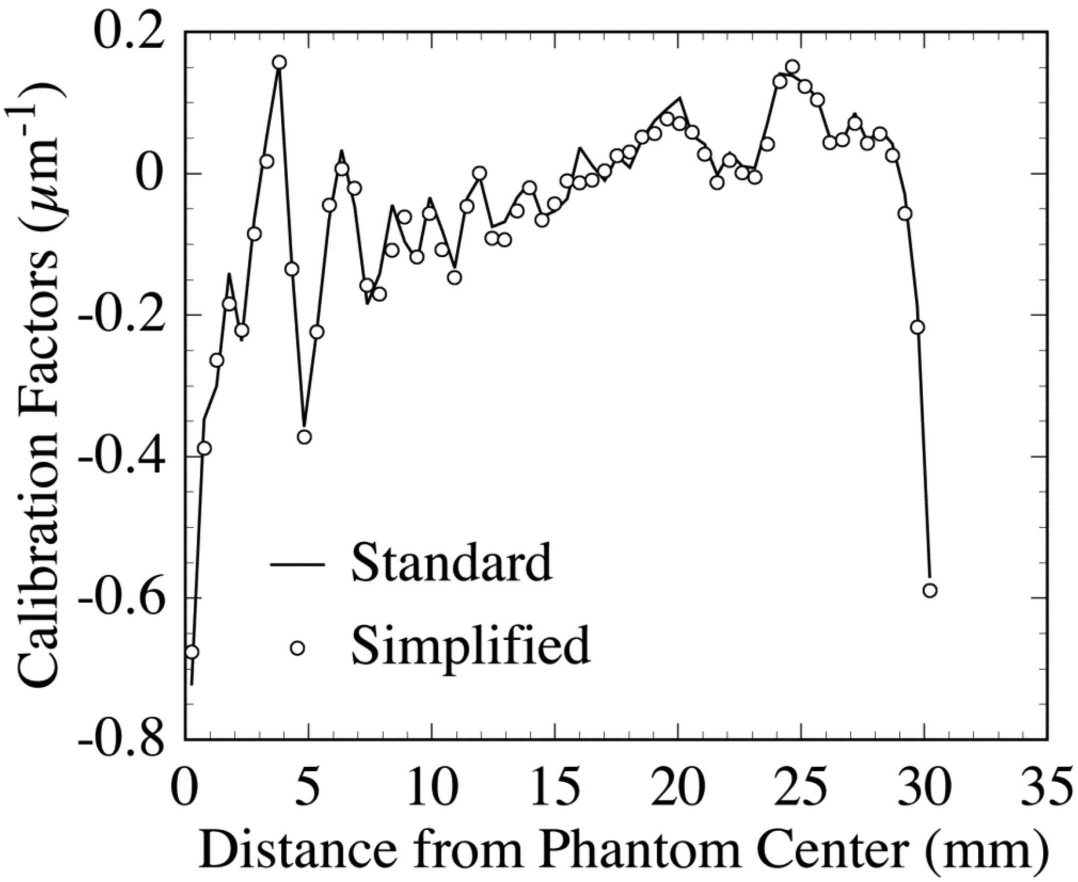

FIG. 4.

Comparison of cupping artifact correction factors obtained with the standard method and with the simplified method (described in the text). The results were obtained using the same detector as that used in Fig. 3. The factors are illustrated as a function of the radial distance from the center of the phantom.

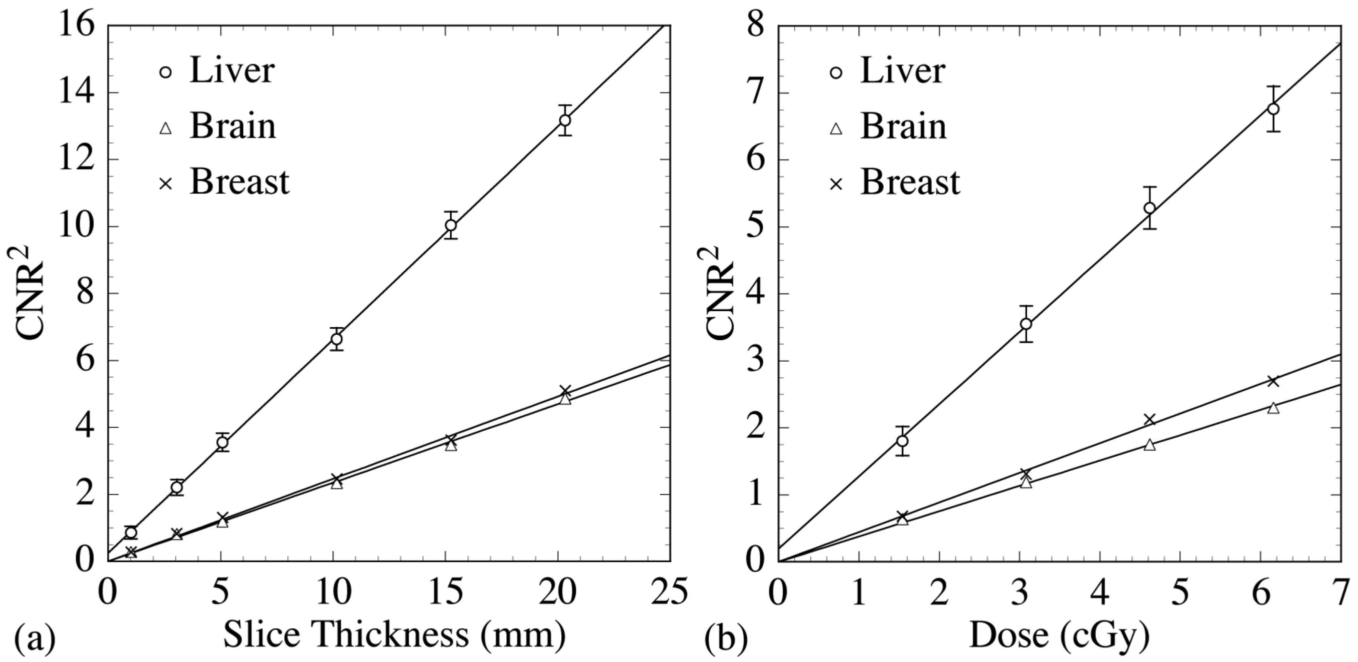

FIG. 5.

CNR^2 as a function of (a) reconstructed slice thickness and (b) total scan dose obtained using the 40 mm thick segmented CsI detector with low density septal walls. The solid lines indicate linear fits to the data. For clarity of presentation, error bars are only shown for the liver-equivalent object. For a given slice thickness or dose, the relative errors in CNR^2 for the other two objects are approximately the same as that for the liver-equivalent object. Note that in this figure and in the remaining figures, the label "dose" refers to the equivalent calibration dose as defined in Sec. II. B. 1.

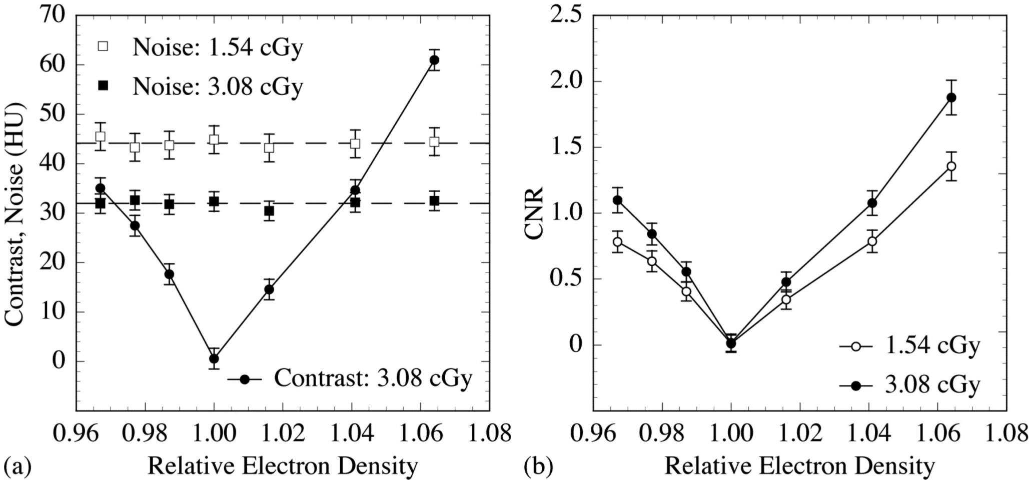

FIG. 6.

Simulation results plotted as a function of the relative electron density of the various tissue-equivalent objects examined in this study. (a) *Contrast* at 3.08 cGy, as well as *Noise* results at 1.54 and 3.08 cGy. The solid line joining the *Contrast* data points is drawn to guide the eye, whereas the dashed lines indicate the mean levels of the *Noise* results at two doses. (b) *CNR* at 1.54 and 3.08 cGy. The solid lines joining the *CNR* data points are drawn to guide the eye.

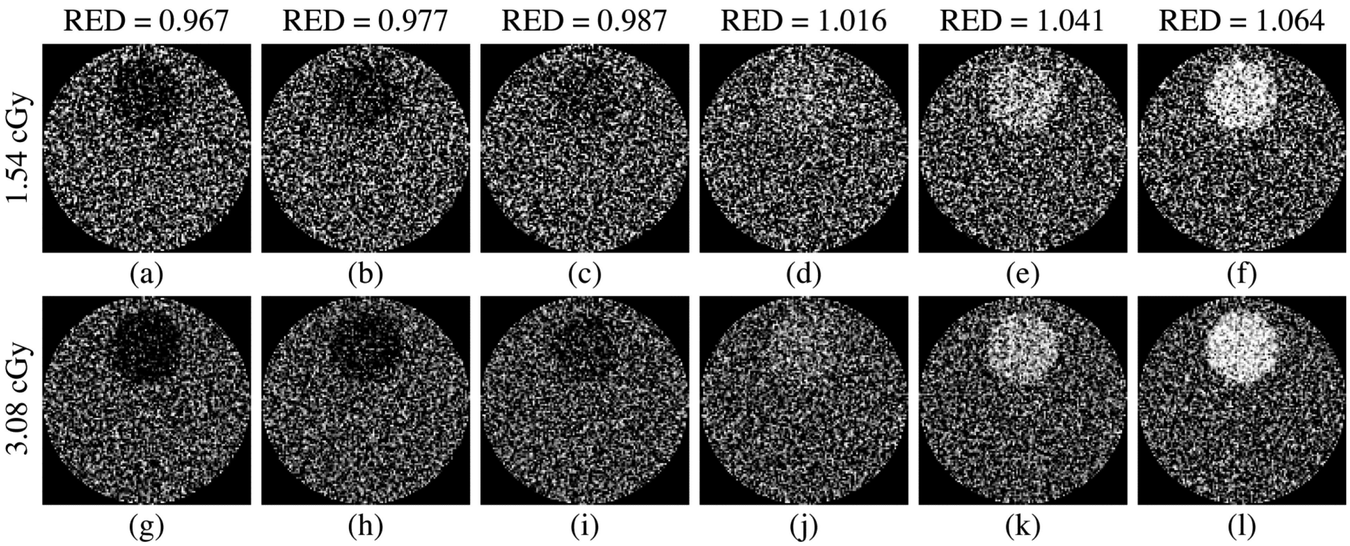

FIG. 7.

Reconstructed images of the CT contrast phantoms embedded with various tissue-equivalent objects. For each phantom, a pair of images obtained at 1.54 cGy and 3.08 cGy is shown. The relative electron densities (RED) of the objects are indicated for each image pairs. The same window level was selected for the images obtained at the same dose, whereas different window levels were selected for different doses in order to maximize the visibility of the objects.

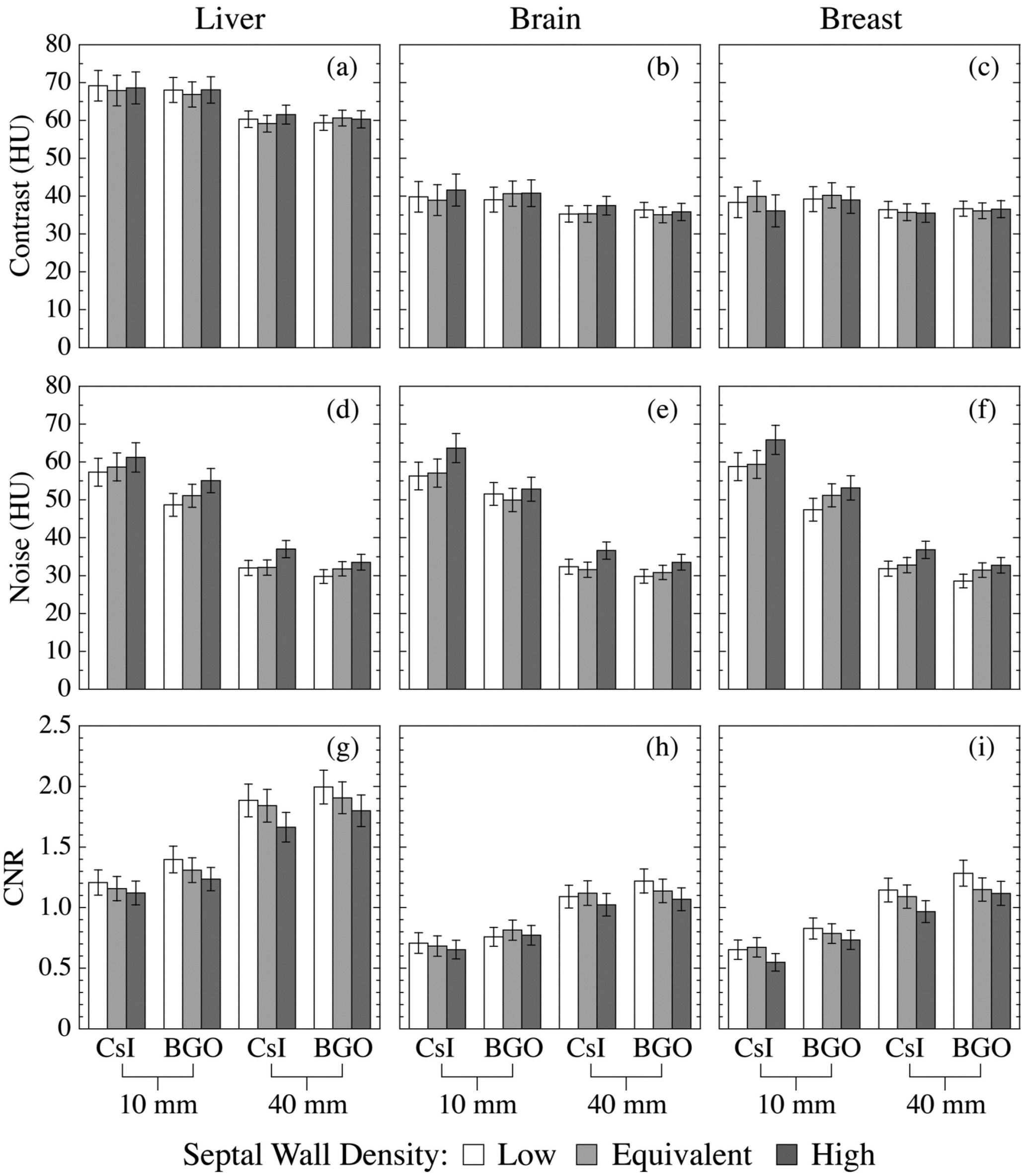

FIG. 8.

Contrast, *Noise* and *CNR* results for the liver-, brain- and breast-equivalent objects obtained using various segmented scintillating detectors. In each figure, the results obtained using the detectors with the same thickness and scintillator material are illustrated in one group. Moreover, in each group, detector designs with different septal wall materials are indicated by columns with different shadings.

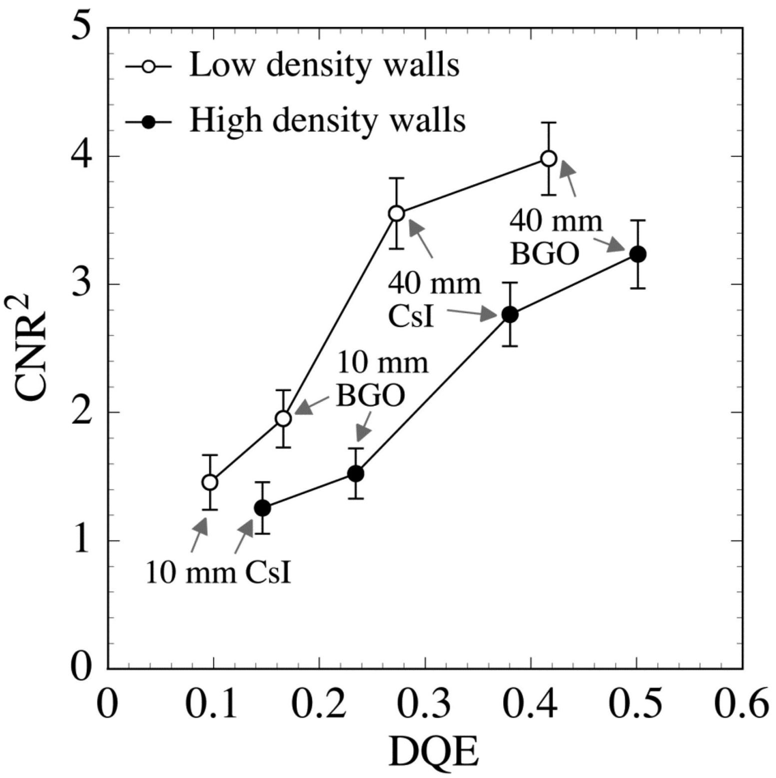

FIG. 9.

CNR^2 results for the liver-equivalent object. These results were obtained using the segmented detectors with low and high density septal walls. The data are plotted as a function of zero frequency *DQE* of the corresponding segmented scintillating detectors. The detector thickness and scintillator material are indicated for each detector. The lines joining the data points are drawn to guide the eye.

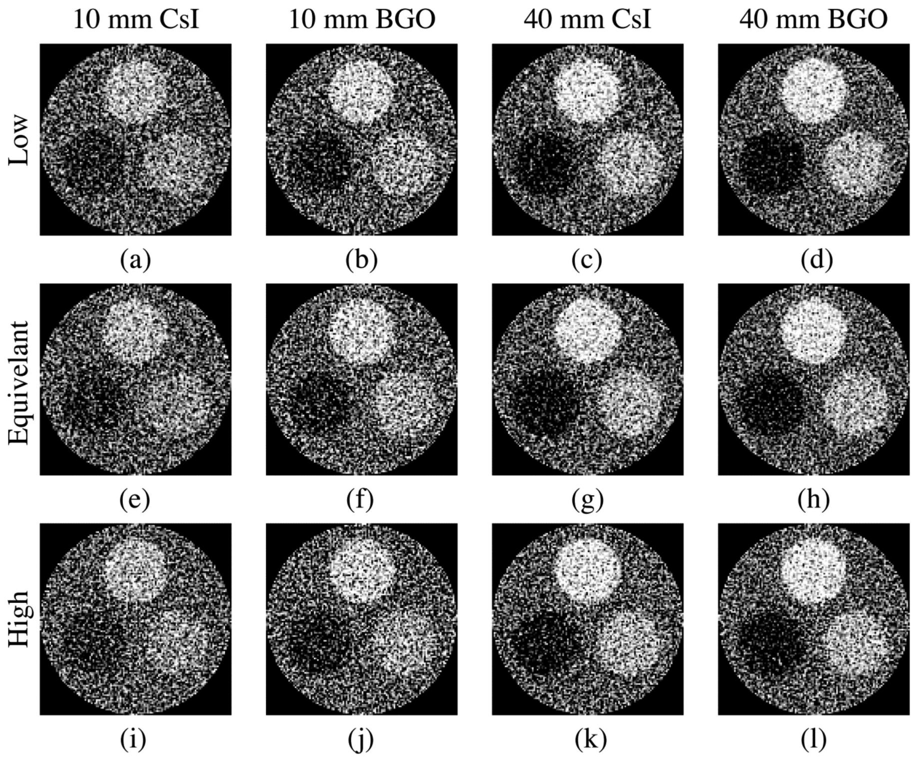

FIG. 10.

Reconstructed images of the three-object phantom obtained using various segmented detectors at 3.08 cGy. Each column represents detectors with a given detector thickness and scintillator material, whereas each row represents detectors with a given type of septal wall density (*i.e.*, “Low”, “Equivalent” and “High”). The orientation of the objects in the phantom is the same as in Fig. 2(b). The same window level was selected for the images in the same column, while different window levels were selected for different columns to maximize the objects visibility.

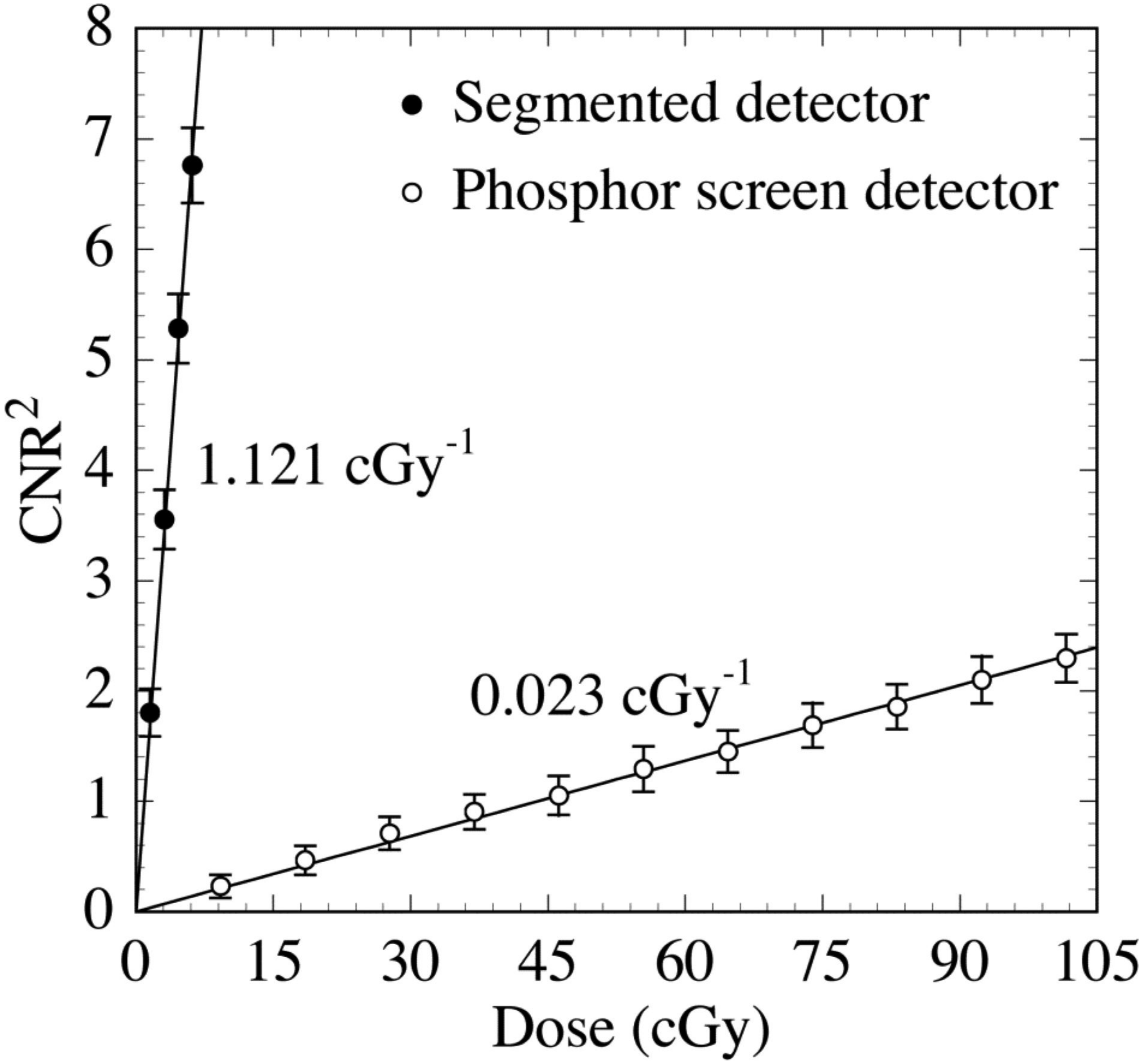

FIG. 11.

CNR^2 results for the liver-equivalent object as a function of total scan dose. Results are shown for the 40 mm thick segmented CsI detector with low density septal walls. Results are also shown for a phosphor detector representative of the type used in conventional MV AMFPIs. The solid lines indicate linear fits to the data. The slope of the linear fit, representing the sensitivity of CNR^2 to dose, is indicated for each detector.

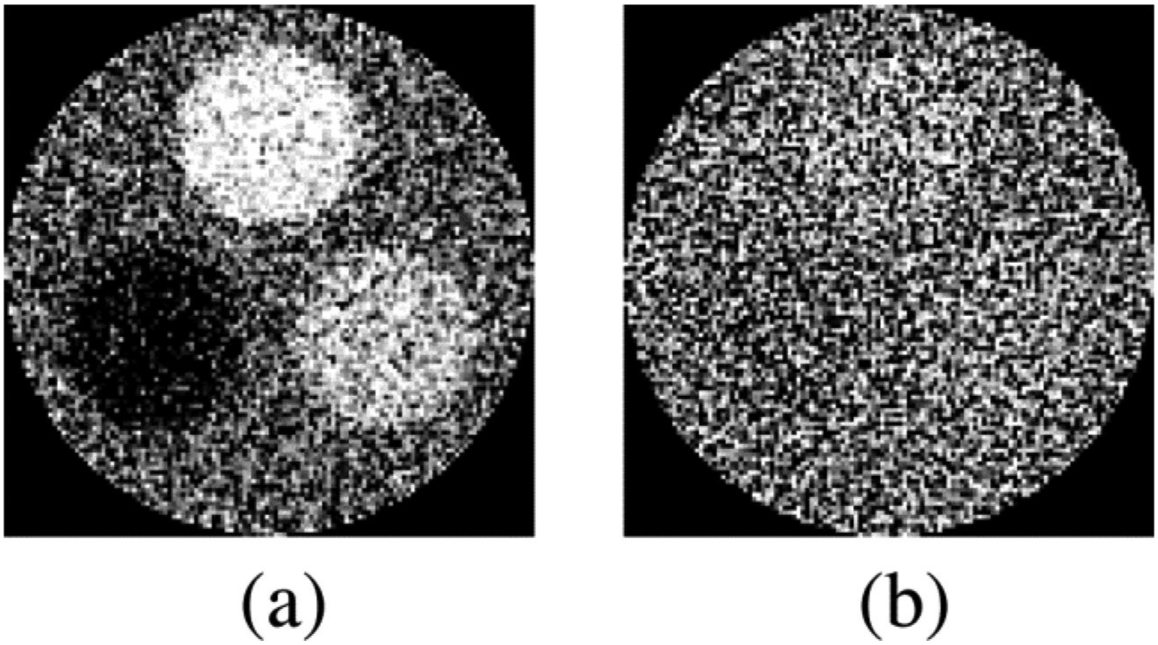

FIG. 12.

Reconstructed images of the three-object phantom obtained at 4.62 cGy using (a) the 40 mm thick segmented CsI detector with low density septal walls, and (b) the phosphor screen detector.

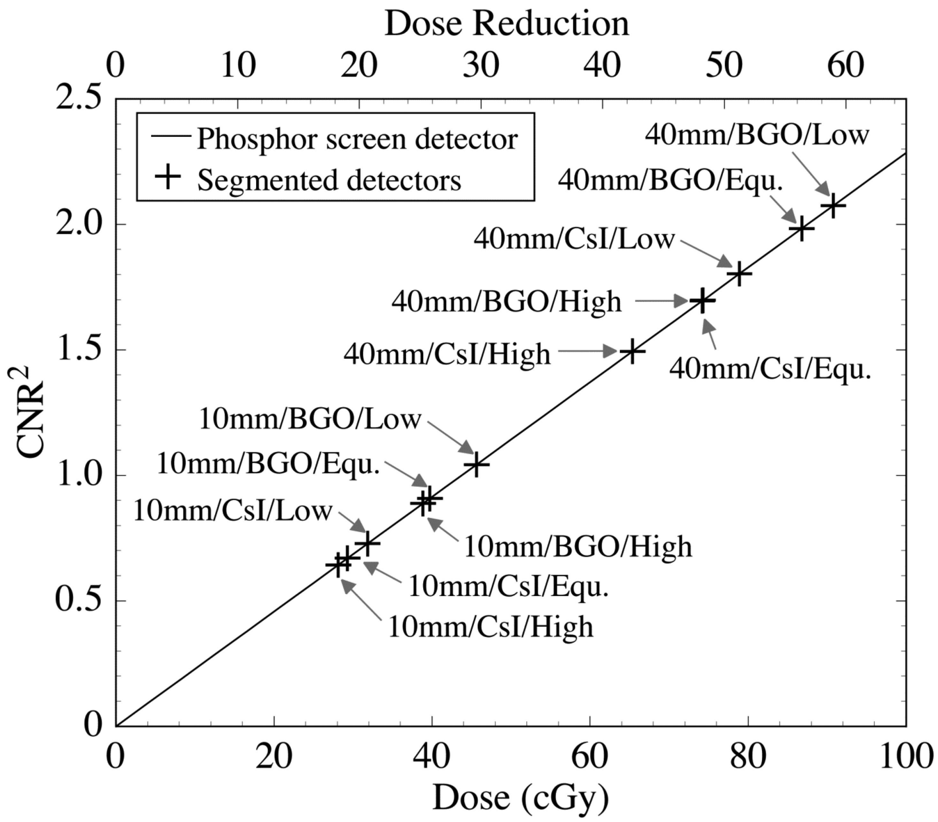

FIG. 13.

Comparison of the CNR^2 performance obtained using the various segmented detectors at 1.54 cGy with that obtained using the phosphor screen detector at much higher doses. The solid line represents the CNR^2 performance of the phosphor screen plotted as a function of dose (bottom x-axis scale). The cross symbols, which represent the CNR^2 values obtained using the various segmented detectors at 1.54 cGy, are positioned along the x-axis direction so as to fall on the phosphor screen performance line. Thus the degree of dose reduction offered by the segmented detectors compared to the phosphor screen is represented by the top x-axis scale. For each segmented detector result, the design parameters of the corresponding detector (“detector thickness/scintillator material/ septal wall density”) are indicated in the figure. Note that “Low”, “Equ.” and “High” refer to the low, equivalent and high density walls used in the simulations. Also note that the results for “40mm/BGO/High” and “40mm/CsI/Equ.” almost exactly overlap.

TABLE I

Chemical compositions by percentage of element weight, physical density and relative electron density of the tissue-equivalent materials examined in this study.

Tissue-equivalent Material	Element Weight (%)										Physical Density (g/cm^3)	Relative Electron Density
	H	C	N	O	Na	P	S	Cl	K	Ca		
Breast (BR12)*	8.68	69.95	2.37	17.91				0.14		0.95	0.990	0.967
Lipoma**	10.90	71.90	3.00	13.80	0.10		0.20	0.10			0.980	0.977
Mammary Gland (Adult #1)**	10.90	50.60	2.30	35.80	0.10	0.10	0.10	0.10			0.990	0.987
Skin (Fetus)**	10.80	5.10	1.20	82.10	0.20	0.10	0.10	0.30	0.10		1.020	1.016
Brain (SR2)*	10.83	72.54	1.69	14.86				0.08			1.045	1.041
Liver (mix)*	8.09	67.00	2.47	19.99				0.14		2.31	1.095	1.064

In the first column, the symbol "*" indicates material information obtained from Ref. [55], while the symbol "**" indicates material information obtained from Ref. [56].

TABLE II

For the various segmented detectors (columns 2 –9) and the phosphor screen detector (column 10), *CNR* results for the liver-equivalent object at 3.08 cGy (CNR_{Liver}) are shown. The *CNR* result for the phosphor screen detector was interpolated from the slope of CNR^2 versus dose results illustrated in Fig. 11. Also shown are *MTF* results at 0.5 and 1.0 line pair/mm ($MTF_{0.5}$ and $MTF_{1.0}$) obtained from a previous study of Monte Carlo simulations of radiation energy deposition involving the same segmented detector configurations.[48] For comparison, *MTF* results obtained from measurements[36] with an MV AMFPI employing a phosphor screen (Lanex Fast B, Eastman Kodak) equivalent to that simulated in the present study are also listed in the last column. Note that, for segmented detectors, the first row indicates the detector thickness and scintillator material, and the second row indicates the septal wall density.

X-ray Detector	**10 mm CsI**		**40 mm CsI**		**10 mm BGO**		**40 mm BGO**		**Phosphor Screen**
	Low	**High**	**Low**	**High**	**Low**	**High**	**Low**	**High**	
CNR_{Liver}	1.21	1.12	1.88	1.66	1.40	1.23	2.00	1.80	0.27
$MTF_{0.5}$	0.41	0.55	0.33	0.46	0.49	0.58	0.39	0.48	0.37
$MTF_{1.0}$	0.20	0.29	0.15	0.26	0.25	0.33	0.19	0.27	0.12